


## EDGE ARTICLE

Cite this: *Chem. Sci.*, 2024, 15, 7308

All publication charges for this article have been paid for by the Royal Society of Chemistry

# Structure-regulated enhanced Raman scattering on a semiconductor to study temperature-influenced enantioselective identification†

Jing Xu,<sup>ab</sup> Junhan Li,<sup>a</sup> Xuao Liu,<sup>a</sup> Xu Hu,<sup>a</sup> Hairihan Zhou,<sup>a</sup> Zhida Gao,<sup>a</sup> Jingwen Xu<sup>\*a</sup> and Yan-Yan Song<sup>†</sup><sup>\*a</sup>

Surface-enhanced Raman scattering (SERS) spectroscopy is an effective technique that can reveal molecular structure and molecular interaction details. Semiconductor-based SERS platforms exhibit multifaceted tunability and unique selectivity to target molecules as well as high spectral reproducibility. However, the detection sensitivity of semiconductors is impeded by inferior SERS enhancement. Herein, a surface and interference co-enhanced Raman scattering (SICERS) platform based on corrugated TiO<sub>2</sub> nanotube arrays (c-TiO<sub>2</sub> NTs) was developed, and the coupling of structural regulation and photo-induced charge transfer (PICT) effectively optimized the SERS performance of the semiconductor substrate. Due to the regularly oscillating optical properties of the c-TiO<sub>2</sub> NTs, well-defined interference patterns were generated and the local electric field was significantly increased, which greatly promoted both the electromagnetic mechanism and PICT processes. The c-TiO<sub>2</sub> NTs were subsequently applied as a highly sensitive SICERS substrate to investigate the mechanism of temperature influence on enantioselective identification. This identification process is related to the existence of temperature-sensitive hydrogen bonds and  $\pi$ - $\pi$  interaction. This work demonstrates a simply prepared, low-cost, and sensitive SERS substrate that enables better investigation into molecular identification.

Received 5th February 2024

Accepted 17th April 2024

DOI: 10.1039/d4sc00855c

rsc.li/chemical-science

## Introduction

Surface-enhanced Raman scattering (SERS) is a powerful technique for trace analysis. SERS offers insights into the chemical structure and composition of molecules, enabling a wide range of potential applications across various fields ranging from nanostructure characterization to biochemical analysis.<sup>1–3</sup> Conventional SERS substrates are based on the electromagnetic mechanism (EM),<sup>4</sup> which utilizes the localized surface plasmon resonance (LSPR) effect of incident light excitation on a rough-surfaced metal to locally amplify an electromagnetic field.<sup>5,6</sup> Typical EM strategies involve the construction of noble metal nanostructures with small gaps to generate “hotspots” and

enhance the Raman scattering of nearby molecules. However, the signals of traditional EM-based SERS substrates significantly fluctuate due to the inherently non-uniform distribution of hotspots in the plasmonic nanostructures, and the poor selectivity of these substrates for target molecules usually results in complicated signal outputs. Another SERS mechanism is the chemical mechanism, which is derived from the efficient photo-induced charge transfer (PICT) that occurs between a substrate and molecules. PICT amplifies both the molecular polarizability tensor and Raman scattering cross-section.<sup>7,8</sup> To date, the cost-effective fabrication, high spectral stability, and repeatability of semiconductors enable them competitive SERS substrates. Unfortunately, owing to their short-range charge transfer (CT) processes, the sensitivity of semiconductor-based SERS substrates is still much lower than that of noble metal-based SERS substrates.

Many strategies have been developed to enhance the performance of semiconductor-based SERS substrates.<sup>9</sup> Among them, defect engineering is a well-established solution that can effectively activate the innate SERS activity of semiconductor-based substrates. Generally, defect engineering alters the band structure, surface properties, and densities of state of semiconductors. This is achieved by using complicated synthesis routes or post-treatment steps to introduce surface defects, which endow semiconductors with enhanced CT efficiency.<sup>10</sup> Moreover, the structure of semiconductors is a crucial

<sup>a</sup>Department of Chemistry, College of Sciences, Northeastern University, Shenyang 110819, China. E-mail: yy-song@mail.neu.edu.cn; xujingwen@mail.neu.edu.cn

<sup>b</sup>State Key Laboratory of Medicinal Chemistry and Molecular Diagnosis of the Ministry of Education, College of Chemistry & Materials Science, Hebei University, Baoding 071002, China

† Electronic supplementary information (ESI) available: The interferometric reflectance spectra, Raman spectra, and SEM images of TiO<sub>2</sub> NTs; Raman measurement of R6G and MB on TiO<sub>2</sub> membrane, s-TiO<sub>2</sub> NTs, and c-TiO<sub>2</sub> NTs; schematic illustrations of preparation of chiral SICERS substrate; SERS spectra for sensing L/D-DOPA under different chiral recognition time, Fe<sup>3+</sup> concentration, and Fe<sup>3+</sup> chelation time; Interferometric reflectance spectra, XPS survey spectra, EDS mapping images, FTIR spectra, zeta potential, and CD spectra of different substrate. See DOI: <https://doi.org/10.1039/d4sc00855c>

factor in enhancing the Raman signal. For example, multiple reflection processes in SERS substrates can lead to light interference, generating interference-enhanced Raman scattering (IERS). By altering the nanostructure, the optical properties of semiconductors such as light reflection, absorption, and interference can be regulated, which affects the electromagnetic field.<sup>14,12</sup> Enhanced light absorption and LSPR at the nanostructure of semiconductors produce an enhanced interaction between different light routes and matter at optical hotspots, where the localized electromagnetic field is maximized. To date, few efforts have been made to integrate nanostructure-designed strategies and PICT processes to broaden the application prospects of semiconductor-based SERS substrates.

TiO<sub>2</sub> nanostructures are typical semiconductor nano-materials that show advantages in terms of stability, economy, and biocompatibility. Among the various forms of TiO<sub>2</sub>, TiO<sub>2</sub> nanotube arrays (TiO<sub>2</sub> NTs) fabricated *via* electrochemical anodization have a regular geometric morphology, making them excellent candidates for use as SERS substrates.<sup>13–16</sup> However, typical TiO<sub>2</sub> NTs show poor SERS activity and are merely used as uniform substrates for plasmonic metal.<sup>17</sup> In our previous work, we found that tailoring the water content of the electrolyte enabled the formation of TiO<sub>2</sub> NTs with a corrugated surface capable of generating an interference signal.<sup>18</sup> The interference of light is related to multiple reflection processes at material interfaces,<sup>19,20</sup> and IERS effects lead to the generation of amplified Raman signals.<sup>21–23</sup> Herein, by combining chemical enhancement and nanostructure regulation strategies, a substrate containing corrugated TiO<sub>2</sub> NTs (c-TiO<sub>2</sub> NTs) with optical interference properties was fabricated by a simple preparation process for use as a surface and interference co-enhanced Raman scattering (SICERS) platform with enhanced sensitivity and high molecular selectivity (Fig. 1). By regulating the nanostructure of the TiO<sub>2</sub> NTs, a concentrated electric field region was generated within hotspots, which facilitated both

the EM effect and the PICT efficiencies of the semiconductor-based SERS substrate. The ultrasensitive and selective c-TiO<sub>2</sub> NTs substrate was subsequently employed to investigate the influence of temperature on enantioselective identification, and the mechanism of this process was clarified. Prussian blue (PB), which had an amplified and interference-free Raman signal, was formed *in situ* on the chiral c-TiO<sub>2</sub> NTs substrate. This enabled the quantitative analysis of 3,4-dihydroxyphenylalanine (L/D-DOPA) enantiomers. The enantioselective identification mechanism was ascertained by investigating the temperature-sensitive hydrogen bonds and  $\pi$ - $\pi$  interactions between the chiral environment and DOPA isomers.

## Results and discussion

### Fabrication and characterization of SICERS substrate

c-TiO<sub>2</sub> NTs with good optical interference properties were prepared *via* electrochemical anodization. During the nanotube formation process, the oscillating optical properties of the nanotubes were determined by the anodic oxidation conditions. The water content of the electrolyte affected the growth rate and etching rate of the nanotubes (*i.e.*, the chemical dissolution rate).<sup>24</sup> Bis(tetrabutylammonium) dihydrogen bis(isothiocyanate) bis(2,2'-bipyridyl-4,4'-dicarboxylate) ruthenium(II) (N719) molecules were selected as Raman probes to optimize the interference pattern of the TiO<sub>2</sub> NTs. The strongest SERS signal, corresponding to the optimal interference conditions, was generated on the c-TiO<sub>2</sub> NTs with a length of 1.73  $\mu\text{m}$  (Fig. S1–S3†). According to our previous work, corrugated nanotube sidewalls are conducive to generating optical interference, and the nanotube sidewall morphology can be regulated by controlling the electrolyte water content.<sup>18</sup> Fig. S4 and S5† show that the TiO<sub>2</sub> NTs grown in an electrolyte with low water content had smooth tube walls, while the walls of the TiO<sub>2</sub> NTs grown in an electrolyte with high water content had corrugated tube

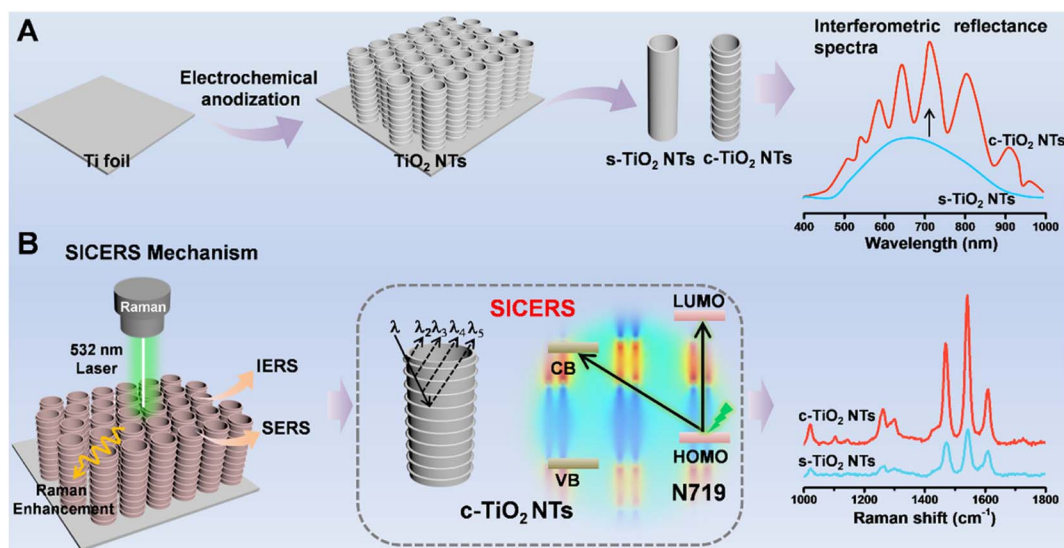


Fig. 1 (A) Schematic illustration of the fabrication of c-TiO<sub>2</sub> NTs SICERS substrate. (B) SICERS mechanism of the c-TiO<sub>2</sub> NTs with significant signal enhancement.

walls. However, excess water in the electrolyte accelerated the etching speed of the fluorine-rich layer between the nanotubes, leading to deformed nanotubes with a spongy appearance. Thus, the optimum water content of the electrolyte was 15% (Fig. S6†).

### SICERS properties and mechanism of c-TiO<sub>2</sub> NTs

To gain the optimal Raman signal, the visible excitation wavelength dependence phenomena was investigated based on the Raman spectra of N719 under 532, 638, and 785 nm excitations (Fig. S7†). Under the 532 nm laser excitation, N719 exhibited the highest Raman signal intensity at the self-assembled monolayers level. Therefore, the 532 nm laser was used the excitation light in the following study. The SICERS properties of the c-TiO<sub>2</sub> NTs and the effect of the TiO<sub>2</sub> NTs tube wall morphology on the SERS signal were evaluated using a TiO<sub>2</sub> nanoparticle-based membrane and TiO<sub>2</sub> NTs with smooth tube walls (s-TiO<sub>2</sub> NTs) as the control (Fig. S8†). The SEM characterizations in Fig. 2A–D show that the c-TiO<sub>2</sub> NTs were composed of parallel and compact nanotubes with tube diameters of ~155 nm. Numerous corrugations were observed on the tube walls of the c-TiO<sub>2</sub> NTs, providing an optical interference phenomenon. Compared with the TiO<sub>2</sub> nanoparticle-based membrane, the s-TiO<sub>2</sub> NTs and c-TiO<sub>2</sub> NTs showed stronger SERS signals after the adsorption of various probe molecules, including N719, 4-aminothiophene (4-ATP), crystal violet (CV), PB, rhodamine 6G (R6G), and methylene blue (MB) (Fig. 2E–H and S9†). The periodically ordered nanotubular structures of the s-TiO<sub>2</sub> NTs

and c-TiO<sub>2</sub> NTs acted as photonic lattices to reflect light at specific frequencies, leading to enhanced Raman signals. Moreover, the periodically ordered nanostructures of the TiO<sub>2</sub> NTs also provided uniform SERS signals, and the Raman spectra collected from 30 random points on a single sample showed a relative standard deviation (RSD) of 3.89% (Fig. 2I and S10A†). Meanwhile, the facile preparation of TiO<sub>2</sub> NTs achieved a high reproducibility of 2.45% across ten different c-TiO<sub>2</sub> NTs samples (Fig. 2J and S10B†). Interestingly, the SERS signals of most of the probe molecules were significantly enhanced by the c-TiO<sub>2</sub> NTs substrate compared with the s-TiO<sub>2</sub> NTs substrate. However, 4-ATP only showed a slight Raman enhancement on the c-TiO<sub>2</sub> NTs substrate (Fig. 2K). A comparison of the Raman intensities of the N719 and 4-ATP peaks is shown in Fig. 2L. The non-symmetric mode of N719 at 1266 cm<sup>-1</sup> ( $\nu(\text{C}=\text{N})$  (bpy) +  $\nu(\text{C}-\text{C})$  intern-ring (bpy) vibration mode) was significantly influenced by the CT process. The Raman shift of N719 at 1022 cm<sup>-1</sup> was attributed to the symmetric vibration of the benzene ring, which was related to the LSPR contribution and was independent of the CT effect. Compared with the s-TiO<sub>2</sub> NTs substrate, these N719 Raman peaks were significantly enhanced by the c-TiO<sub>2</sub> NTs substrate. However, for 4-ATP, only a slight Raman enhancement was observed for the EM-affected peak at 1087 cm<sup>-1</sup>, while the CT influenced peak at 1593 cm<sup>-1</sup> showed a negligible change in intensity. Based on the peak intensity of N719 at 1474 cm<sup>-1</sup> on a silicon wafer and c-TiO<sub>2</sub> NTs (Fig. S11†), the enhancement factors (EFs) of c-TiO<sub>2</sub> NTs were estimated to be  $6.1 \times 10^4$ . Although the EFs of c-TiO<sub>2</sub> NTs were lower than some two-dimensional semiconducting materials

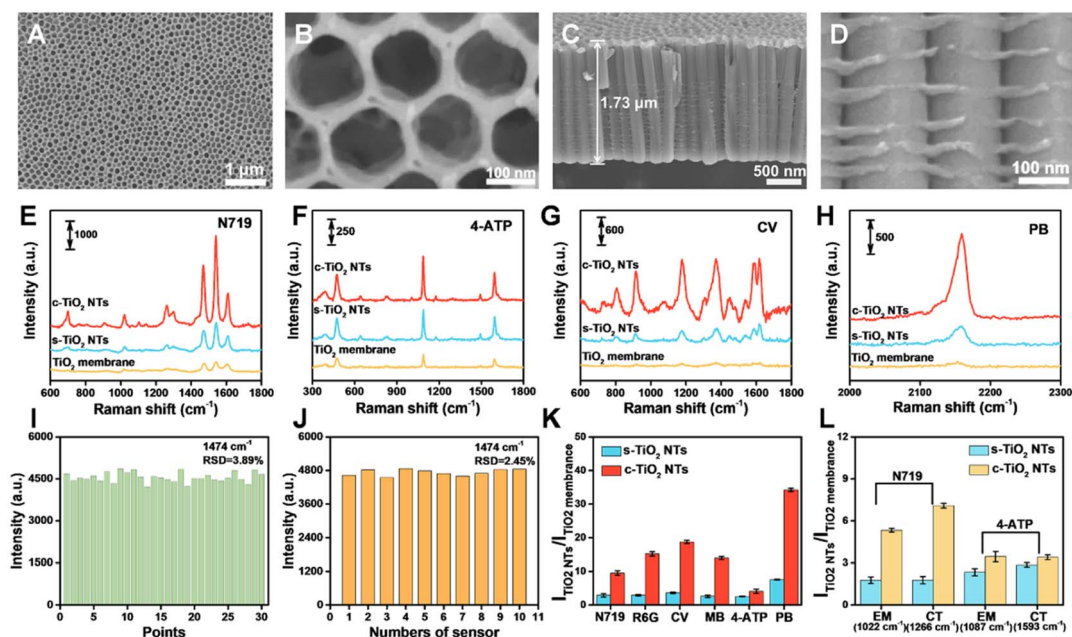


Fig. 2 SEM images of (A and B) top view and (C and D) side view of c-TiO<sub>2</sub> NTs prepared using an electrolyte with 15% water content. Raman measurement of (E) N719, (F) 4-ATP, (G) CV, and (H) PB on TiO<sub>2</sub> membrane, s-TiO<sub>2</sub> NTs, and c-TiO<sub>2</sub> NTs. (I) Signal intensity of N719 at 1474 cm<sup>-1</sup> collected from thirty random points on c-TiO<sub>2</sub> NT-based substrates to demonstrate uniformity. (J) Signal intensity of N719 at 1474 cm<sup>-1</sup> collected on ten different c-TiO<sub>2</sub> NTs samples to demonstrate reproducibility. (K) Raman intensity ratios of N719, R6G, CV, MB, 4-ATP, and PB on the surfaces of the s-TiO<sub>2</sub> NTs and c-TiO<sub>2</sub> NTs to the TiO<sub>2</sub> membrane. (L) Raman intensity ratios of N719 (at 1022 cm<sup>-1</sup> and 1266 cm<sup>-1</sup>) and 4-ATP (at 1087 cm<sup>-1</sup> and 1593 cm<sup>-1</sup>) on the surface of the s-TiO<sub>2</sub> NTs and c-TiO<sub>2</sub> NTs to the TiO<sub>2</sub> membrane.



like MXenes and graphitic carbon, *c*-TiO<sub>2</sub> NTs exhibited high-lights as good reproducibility, stability, and tailorability.

To investigate the enhanced SERS performance of the *c*-TiO<sub>2</sub> NTs compared to the *s*-TiO<sub>2</sub> NTs, the penetration process of the incident laser on the substrates was evaluated. According to the SERS mechanism, in Fig. 3A the collective excitation of electron gas or surface plasma of the conductor (in this case, the Ti substrate) was confined near the Ti/*c*-TiO<sub>2</sub> NTs interface, and the light at the interface was significantly amplified under surface plasma excitation. As a result, both the incident radiation and reflected radiation at the Ti/*c*-TiO<sub>2</sub> NTs interface were enhanced. According to the IERS mechanism, both the surface-enhanced reflected radiation and incident radiation contributed to the overall Raman scattering process in the IERS system, leading to a significant enhancement in SERS signal intensity. The finite difference time domain (FDTD) results in Fig. 3B and C show that the locally enhanced electric field of the *c*-TiO<sub>2</sub> NTs presented a periodic distribution along the nanotubes (in the *z*-direction), and the field strength was significantly higher than that of the *s*-TiO<sub>2</sub> NTs. Compared to the *s*-TiO<sub>2</sub> NTs, stronger electromagnetic oscillation coupling between nanotubes was achieved in the *c*-TiO<sub>2</sub> NTs, which generated more hotspots in the substrate. Meanwhile, due to the periodic arrangement of the *c*-TiO<sub>2</sub> NTs nanostructure, multiple light scattering between nanotube voids improved the light-matter interaction and increased the probability of Raman scattering.<sup>25,26</sup> Therefore, a concentrated electric field region was formed within the *c*-TiO<sub>2</sub> NTs nanostructure due to scattering and interference effects, which was also crucial for its light-harvesting properties.

The enhanced SERS performance of the *c*-TiO<sub>2</sub> NTs for different molecules was further evaluated. The direct band gap ( $E_g$ ) of *c*-TiO<sub>2</sub> NTs was determined to be  $\sim 3.50$  eV by Tauc plots analysis based on the UV-vis absorption spectrum (Fig. S12<sup>†</sup>). Both the non-symmetric bond and symmetric bands of N719 were significantly enhanced by the *c*-TiO<sub>2</sub> NTs compared to the *s*-TiO<sub>2</sub> NTs. As shown in Fig. 3D, under 532 nm (2.3 eV) light excitation, electrons were potentially transferred *via* two routes: (1) from the highest occupied molecular orbital (HOMO) of the prototype molecule N719 ( $-5.34$  eV) to the conduction band (CB,  $-3.45$  eV) of the *c*-TiO<sub>2</sub> NTs; 2) from the HOMO to the lowest unoccupied molecular orbital (LUMO,  $-3.10$  eV) of N719. In this case, the enhanced electric fields between the nanotubes in the *c*-TiO<sub>2</sub> NTs substrate improved both the EM-based Raman scattering and facilitated effective PICT processes in the N719/*c*-TiO<sub>2</sub> NTs system. Consequently, this system exhibits a significantly enhanced CT-based Raman signal compared to the N719/*s*-TiO<sub>2</sub> NTs system. In contrast, the 4-ATP/TiO<sub>2</sub> systems had unmatched band levels. Therefore, the CT process did not occur, and the *c*-TiO<sub>2</sub> NTs only showed insignificant Raman enhancement compared to the *s*-TiO<sub>2</sub> NTs (Fig. 3E). The other probe molecules that had matched energy levels with the *c*-TiO<sub>2</sub> NTs also exhibited distinct enhanced SERS signals on the *c*-TiO<sub>2</sub> NTs when compared to the *s*-TiO<sub>2</sub> NTs (Fig. S13<sup>†</sup>). These results confirmed the vital impact of the hotspots generated by electromagnetic oscillation coupling between nanotubes in PICT processes.

### Construction of SICERS substrate for temperature-influenced enantioselective identification

Identifying enantiomers and elucidating the recognition mechanism of an enantiomer identification strategy are significant challenges in bioanalysis because enantiomers have identical molecular formulas and chemical properties.<sup>27–29</sup> Herein, the simple fabrication of *c*-TiO<sub>2</sub> NTs SICERS substrates with high stability and reproducibility motivated us to develop a platform for investigating the mechanism of enantioselective identification. A chiral environment based on the *c*-TiO<sub>2</sub> NTs was constructed to explore the effect of temperature on enantiomer (*L/D*-DOPA) identification (Fig. 4A and S14<sup>†</sup>). The characterization of this analysis platform (Fig. S15–S21<sup>†</sup>) demonstrated that the prepared *L/D*-Phe/O-Phos/*c*-TiO<sub>2</sub> NTs SICERS substrates were constructed successfully with homochirality. Fig. S22<sup>†</sup> shows the construction of the chiral recognition signal amplification sensing platform. After *L/D*-DOPA identification, an Fe<sup>3+</sup>-DOPA complex was formed *in situ* through chelation between Fe<sup>3+</sup> and the phenol hydroxyl group of DOPA.<sup>15</sup> Fe<sup>3+</sup> subsequently reacted with [Fe(CN)<sub>6</sub>]<sup>4-</sup> to form PB nanocrystals. The selective recognition of DOPA enantiomers on the chiral SICERS substrate was determined by comparing the peak intensity of PB at 2158 cm<sup>-1</sup>. Considering that the DOPA molecules tend to self-polymerize in a basic solution,<sup>30,31</sup> an acidic environment was thus chosen to ensure the DOPA monomer to be recognized on the substrate. To obtain the apparent recognition results, the reaction conditions were optimized as follows: the chiral recognition time was

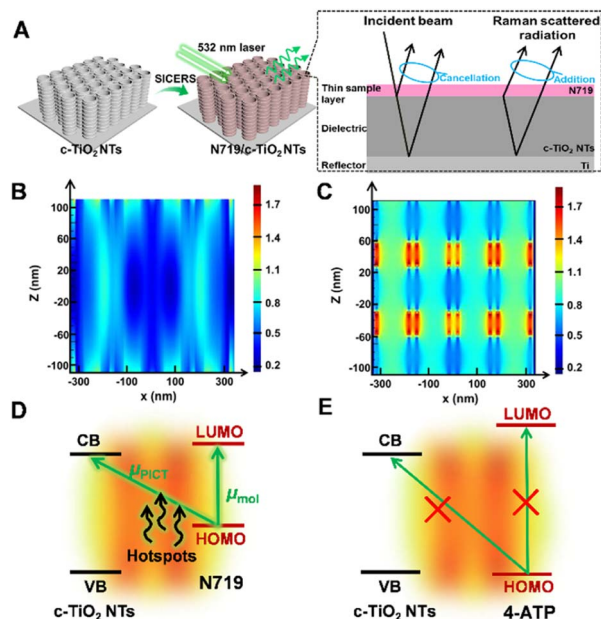


Fig. 3 (A) Schematic diagram illustrating the SICERS effect of the *c*-TiO<sub>2</sub> NTs and generation of Raman signal. Electromagnetic field enhancement images showing vertical sections of (B) *s*-TiO<sub>2</sub> NTs and (C) *c*-TiO<sub>2</sub> NTs. Energy level diagram and CT pathway of (D) N719 and (E) 4-ATP adsorbed on *c*-TiO<sub>2</sub> NTs.

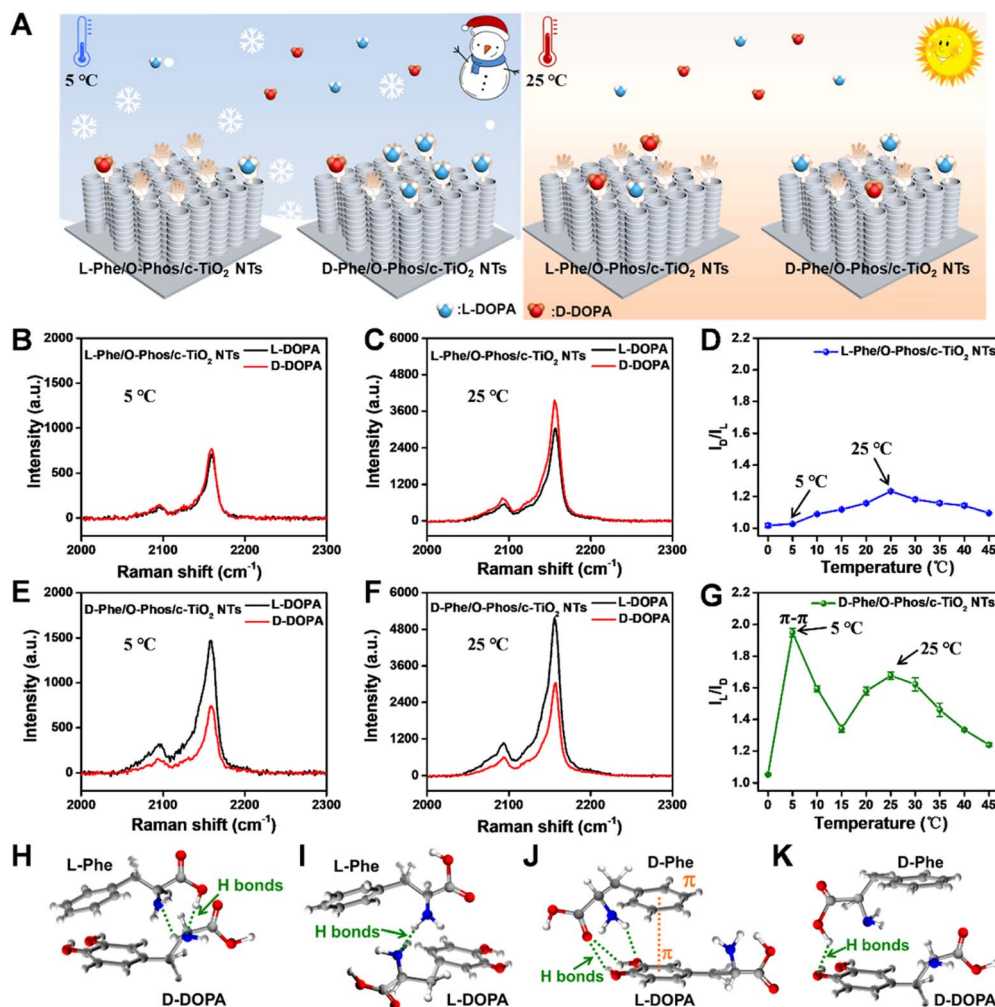


Fig. 4 (A) Schematic illustrations showing the recognition of DOPA enantiomers by the L-Phe/O-Phos/c-TiO<sub>2</sub> NTs and D-Phe/O-Phos/c-TiO<sub>2</sub> NTs substrates at 5 °C and 25 °C. Raman spectra of PB after L/D-DOPA recognition by L-Phe/O-Phos/c-TiO<sub>2</sub> NTs substrate at (B) 5 °C and (C) 25 °C. (D) Influence of temperature on the recognition of L/D-DOPA by the L-Phe/O-Phos/c-TiO<sub>2</sub> NTs substrate. Raman spectra of PB after L/D-DOPA recognition by D-Phe/O-Phos/c-TiO<sub>2</sub> NTs substrate at (E) 5 °C and (F) 25 °C. (G) Influence of temperature on the recognition of L/D-DOPA by the D-Phe/O-Phos/c-TiO<sub>2</sub> NTs substrate. Energy-minimized dominant interaction models (ball-and-stick) of (H) L-Phe with D-DOPA, (I) L-Phe with L-DOPA, (J) D-Phe with L-DOPA, and (K) D-Phe with D-DOPA.

60 min, the Fe<sup>3+</sup> concentration was 0.5 mM, and the Fe<sup>3+</sup> chelation time was 30 min (Fig. S23–S25†). To determine the influence of electrostatically adsorbed Fe<sup>3+</sup> ions on DOPA sensing, we also explored the PB generation ability induced by the adsorbed Fe<sup>3+</sup> ions on c-TiO<sub>2</sub> NTs, O-Phos/c-TiO<sub>2</sub> NTs, and L-Phe/O-Phos/c-TiO<sub>2</sub> NTs (Fig. S26†). Apparently, very weak PB signals were detected on these samples, indicative the effective PB-growth strategy by using the recognized L/D-DOPA.

Previous studies have shown that the hydrogen bonds between the L/D-Phe and L/D-DOPA is crucial for the chiral recognition process, and the strength of this hydrogen bond is closely related to temperature.<sup>32</sup> As predicted, chiral substrates exhibited different chiral recognition phenomena at different recognition temperatures (Fig. 4B–D). The PB Raman signal intensities obtained for the same concentrations of L/D-DOPA on the L-Phe/O-Phos/c-TiO<sub>2</sub> NTs substrate at 5 °C significantly overlapped, suggesting that the target enantiomer was not able

to be distinguished using the homochiral substrate at a low temperature. At 25 °C, the PB Raman intensity generated after D-DOPA identification by the L-Phe/O-Phos/c-TiO<sub>2</sub> NTs substrate was higher than that of L-DOPA. For the D-Phe/O-Phos/c-TiO<sub>2</sub> NTs substrate (Fig. 4E–G), the PB Raman intensities after recognizing L-DOPA at both 5 °C and 25 °C were significantly higher than that of D-DOPA. To understand the chiral recognition behavior of the substrates under different temperatures, chiral recognition based on L-Phe and D-Phe was examined at a range of temperatures from 0 to 45 °C (Fig. 4D and G). The results indicated that chiral selectivity for the DOPA enantiomer depended on the experimental temperature. The selectivity of the L-Phe/O-Phos/c-TiO<sub>2</sub> NTs chiral sensor for D-DOPA increased with increasing temperature, and this chiral sensor exhibited the highest selectivity for D-DOPA, especially at 25 °C. Meanwhile, the D-Phe/O-Phos/c-TiO<sub>2</sub> NTs chiral sensor showed high selectivity at both 5 °C and 25 °C. For other chiral molecules

containing phenolic hydroxyl groups (such as *L/D*-adrenaline), the temperature also affected the chiral recognition process (Fig. S27†).

The interactions between the *L/D*-Phe and DOPA enantiomers were then investigated, as schematically shown in Fig. 4H–K. Both DOPA enantiomers interacted with *L/D*-Phe and formed hydrogen bonds. For *L*-Phe/O-Phos/*c*-TiO<sub>2</sub> NTs, the interaction between *D*-DOPA and *L*-Phe involved the formation of two hydrogen bonds, while the interaction between *L*-DOPA and *L*-Phe formed one hydrogen bond. While for *D*-Phe/O-Phos/*c*-TiO<sub>2</sub> NTs, *L*-DOPA bonded to *D*-Phe through three hydrogen bonds and  $\pi$ - $\pi$  interaction, and *D*-Phe bonded to *D*-DOPA *via* only one hydrogen bond. Therefore, the temperature-influenced chiral recognition process was essentially decided by the different binding modes between the *L/D*-Phe and DOPA enantiomers. Low temperatures are favorable for  $\pi$ - $\pi$  interaction, but molecular motion is limited at low temperatures. However, hydrogen bonds are significantly inhibited due to the limited molecular motion at low temperatures.<sup>33,34</sup> Thus, with increasing temperature, the hydrogen bonds became more prominent, which enhanced the *D*-DOPA selectivity on the *L*-Phe/O-Phos/*c*-TiO<sub>2</sub> NTs substrate (Fig. 4D). The *D*-Phe/O-Phos/*c*-TiO<sub>2</sub> NTs substrate exhibited higher selectivity for *L*-DOPA at low temperatures, especially at 5 °C (Fig. 4G). This was attributed to the stable  $\pi$ - $\pi$  interactions between *D*-Phe and *L*-DOPA at low temperatures. Molecular motion accelerates with increasing temperature due to the weakened intramolecular interactions. Thus, at 25 °C, the formation of hydrogen bonds between *D*-Phe and *L*-DOPA was enhanced. However, excessively high temperatures (30–45 °C) broke the stable hydrogen bonds between the *L/D*-Phe and DOPA enantiomers, resulting in a subsequent decline in recognition efficiency.

The quantitative analysis capability of *L*-Phe/O-Phos/*c*-TiO<sub>2</sub> NTs was investigated (Fig. S28†). The PB Raman signal recorded on the SICERS platform exhibited good linear relationships in the *L/D*-DOPA concentration ranging from 10<sup>-10</sup> to 10<sup>-5</sup> M with the limit of detection (LOD, defined as the mean of blank +3 $\sigma$ ,  $\sigma$  is the standard deviation of blank) of 1.3 × 10<sup>-11</sup> M for *L*-DOPA and 1.0 × 10<sup>-11</sup> M for *D*-DOPA. The X-ray diffraction (XRD) patterns and SEM images also provided the solid evidence for the of PB formation on the surface of *c*-TiO<sub>2</sub> NTs by the DOPA enantiomer recognition process (Fig. S29 and S30†). In addition, the selectivity of the SICERS platform was further evaluated by discriminating other enantiomers, including *L/D*-tryptophan (*L/D*-Trp), *L/D*-carnitine, *L/D*-tyrosine (*L/D*-Tyr), *L/D*-glutamic acid (*L/D*-Glu), and *L/D*-cysteine (*L/D*-Cys) (Fig. S31†). Owing to no phenolic hydroxyl groups in the structures of these enantiomers, Fe<sup>3+</sup> ions cannot be trapped, and thus no obvious PB signal was recorded. The above results confirm the excellent quantitative ability of the as-proposed SICERS platform for DOPA enantiomers.

## Experimental

### Preparation of TiO<sub>2</sub> NTs

Ti foils (15 mm × 15 mm × 0.1 mm) were sequentially cleaned by ultrasonication in isopropanol, ethanol, and deionized

water, then dried under a flow of N<sub>2</sub>. The *c*-TiO<sub>2</sub> NTs with optical interference properties were fabricated by electrochemical anodization.<sup>18,24</sup> Briefly, each Ti foil was anodized at 60 V for 40 min in an electrolyte containing 0.5 wt% NH<sub>4</sub>F and varying water content to prepare the *c*-TiO<sub>2</sub> NTs.

### Preparation of *L/D*-Phe/O-Phos/*c*-TiO<sub>2</sub> NTs

The as-formed *c*-TiO<sub>2</sub> NTs were first functionalized with O-Phos by immersion in a 10 mM O-Phos aqueous solution at 4 °C for 12 h. Subsequently, chiral recognition molecules (*L/D*-Phe) were introduced onto the prepared O-Phos/*c*-TiO<sub>2</sub> NTs using a classic *N*-(3-dimethylaminopropyl)-nethylcarbodiimide hydrochloride (EDC)/*N*-hydroxysulfosuccinimide (NHS) coupling reaction. To link *L/D*-Phe onto the O-Phos/*c*-TiO<sub>2</sub> NTs, 1 mM *L/D*-Phe was dissolved in deionized water containing 10 mg mL<sup>-1</sup> EDC and 5 mg mL<sup>-1</sup> NHS. This mixture was reacted for 30 min to activate the carboxyl group of *L/D*-Phe. The O-Phos/*c*-TiO<sub>2</sub> NTs were soaked in this solution for 12 h at room temperature to obtain the *L/D*-Phe/O-Phos/*c*-TiO<sub>2</sub> NTs.

### Temperature induced chiral recognition for *L/D*-DOPA

Firstly, the as-prepared *L/D*-Phe/O-Phos/*c*-TiO<sub>2</sub> NTs were immersed in *L/D*-DOPA (pH 5.5) aqueous solution at different temperatures for 60 min. After immersion, the substrates were cleaned with deionized water three times to remove uncombined *L/D*-DOPA molecules. The cleaned samples were then incubated in 0.5 mM FeCl<sub>3</sub> aqueous solution for 30 min to fix Fe<sup>3+</sup>. Subsequently, PB was formed by immersing the samples in a 0.5 mM K<sub>4</sub>[Fe(CN)<sub>6</sub>] aqueous solution at room temperature for 30 min.

### Raman measurement

The *c*-TiO<sub>2</sub> NTs were immersed in a 1 mM ethanol solution containing N719 and reacted at 70 °C for 12 h. Raman spectra were recorded using a 532 nm laser (10% power) equipped with a 50× long-distance objective and a spot size of 1  $\mu$ m. The data acquisition time was 10 s, the confocal hole size was 500  $\mu$ m, and the slit aperture size was 200  $\mu$ m. The spectrometer was calibrated using the Raman signal from a silicon wafer at 520.7 cm<sup>-1</sup>. For each measurement, Raman spectra were collected from five different locations to determine the average signal strength.

### Calculation of the electromagnetic surface enhancement in TiO<sub>2</sub> NTs geometries

The field intensity distribution of the *c*-TiO<sub>2</sub> NTs and *s*-TiO<sub>2</sub> NTs was calculated by FDTD. The experimental parameters for the calculations were obtained from the SEM images of the *c*-TiO<sub>2</sub> NTs and *s*-TiO<sub>2</sub> NTs. In the FDTD simulations, four TiO<sub>2</sub> NTs were used as the model, 0.3 nm was used as a unit, and a 532 nm laser was used to irradiate the model along the *z* and *y* axes.



## Conclusions

In summary, a c-TiO<sub>2</sub> NTs substrate with a facilely tailorable nanostructure was proposed in this work as a SICERS platform due to its enhanced Raman scattering properties. This platform was employed to investigate the influence of temperature on enantioselective identification and the mechanism of this influence. By regulating the TiO<sub>2</sub> NTs nanostructure, an enhanced electric field with interference properties was generated in the c-TiO<sub>2</sub> NTs, facilitating both the EM and PICT processes in the semiconductor-based SERS substrate. A signal amplification strategy involving the *in situ* formation of PB was employed to determine that temperature-sensitive hydrogen bonds and  $\pi$ - $\pi$  interactions between the chiral environment of the substrate and isomers were the key to enantioselective recognition. This work offers new opportunities for improving the sensitivity of semiconductor-based SERS substrates with simple methods and is expected to be helpful for biochemical analysis, catalyst monitoring, and material determination.

## Data availability

All the data supporting this article have been included in the main text and the ESI.†

## Author contributions

Y.-Y. Song and J. W. Xu conceived the concept and directed the project. J. Xu performed experiments, analyzed data, and wrote the manuscript. J. H. Li, X. Hu, H. R. H. Zhou performed the experiments. X. A. Liu carried out the theoretical study. Z. D. Gao collected and analyzed the data. All the authors discussed the results and assisted during the manuscript preparation.

## Conflicts of interest

There are no conflicts to declare.

## Acknowledgements

This work was supported by the National Natural Science Foundation of China (No. 22074013, 22374015, and 22204016) and Liaoning Provincial Natural Science Foundation (LJKQZ2021001). Special thanks are due to the instrumental or data analysis from Analytical and Testing Center, Northeastern University.

## Notes and references

- 1 C. Zong, M. X. Xu, L. J. Xu, T. Wei, X. Ma, X. S. Zheng, R. Hu and B. Ren, *Chem. Rev.*, 2018, **118**, 4946–4980.
- 2 M. F. Cardinal, E. V. Ende, R. A. Hackler, M. O. McAnally, P. C. Stair, G. C. Schatz and R. P. Van Duyne, *Chem. Soc. Rev.*, 2017, **46**, 3886–3903.
- 3 G. Song, W. B. Gong, S. Cong and Z. G. Zhao, *Angew. Chem., Int. Ed.*, 2021, **60**, 5505–5511.
- 4 S. Y. Ding, E. M. You, Z. Q. Tian and M. Moskovits, *Chem. Soc. Rev.*, 2017, **46**, 4042–4076.
- 5 L. A. Lane, X. M. Qian and S. M. Nie, *Chem. Rev.*, 2015, **115**, 10489–10529.
- 6 Q. Zhao, H. Hilal, J. Kim, W. Park, M. Haddadnezhad, J. Lee, W. Park, J. W. Lee, S. Lee, I. Jung and S. Park, *J. Am. Chem. Soc.*, 2022, **144**, 13285–13293.
- 7 S. Cong, X. H. Liu, Y. X. Jiang, W. Zhang and Z. G. Zhao, *Int. J. Innov.*, 2020, **1**, 100051.
- 8 X. T. Wang and L. Guo, *Angew. Chem., Int. Ed.*, 2020, **59**, 4231–4239.
- 9 G. Song, S. Cong and Z. G. Zhao, *Chem. Sci.*, 2022, **13**, 1210–1224.
- 10 J. Lin, Y. Shang, X. X. Li, J. Yu, X. T. Wang and L. Guo, *Adv. Mater.*, 2017, **29**, 1604797.
- 11 X. L. Zhu, C. Vannahme, E. H. Nielsen, N. A. Mortensen and A. Kristensen, *Nat. Nanotechnol.*, 2016, **11**, 325–329.
- 12 T. Kim, J. Lee, E. S. Yu, S. Lee, H. Woo, J. Kwak, S. Chung, I. Choi and Y. S. Ryu, *Small*, 2023, **19**, 2207003.
- 13 J. W. Xu, C. C. Liang, Z. D. Gao and Y. Y. Song, *Chin. Chem. Lett.*, 2023, **34**, 107863.
- 14 J. L. Guo, X. A. Liu, J. J. Zhao, H. J. Xu, Z. D. Gao, Z.-Q. Wu and Y.-Y. Song, *Chem. Sci.*, 2023, **14**, 1742–1751.
- 15 J. Xu, Y. F. Xue, X. X. Jian, Y. Zhao, Z. Q. Dai, J. W. Xu, Z. D. Gao, Y. Mei and Y. Y. Song, *Chem. Sci.*, 2022, **13**, 6550–6557.
- 16 L. L. Yang, J. J. Feng, J. N. Wang, Z. D. Gao, J. W. Xu, Y. Mei and Y. Y. Song, *Chin. Chem. Lett.*, 2022, **33**, 5169–5173.
- 17 L. L. Yang, C. X. Zhao, J. W. Xu, J. L. Guo, Z. D. Gao and Y. Y. Song, *Chem. Commun.*, 2020, **56**, 10333–10336.
- 18 Y. Y. Song and P. Schmuki, *Electrochem. Commun.*, 2010, **12**, 579–582.
- 19 G. A. N. Connell, R. J. Nemanich and C. C. Tsai, *Appl. Phys. Lett.*, 1980, **36**, 31–33.
- 20 R. J. Nemanich, C. C. Tsai and G. A. N. Connell, *Phys. Rev. Lett.*, 1980, **44**, 273–276.
- 21 X. Ling and J. Zhang, *J. Phys. Chem. C*, 2011, **115**, 2835–2840.
- 22 L. B. Gao, W. C. Ren, B. L. Liu, R. Saito, Z. S. Wu, S. S. Li, C. B. Jiang, F. Li and H. M. Cheng, *ACS Nano*, 2009, **3**, 933–939.
- 23 N. Jung, A. C. Crowther, N. Kim, P. Kim and L. Brus, *ACS Nano*, 2010, **4**, 7005–7013.
- 24 P. Roy, S. Berger and P. Schmuki, *Angew. Chem., Int. Ed.*, 2011, **50**, 2904–2939.
- 25 J. D. Joannopoulos, P. R. Villeneuve and S. H. Fan, *Nature*, 1997, **386**, 143–149.
- 26 C. T. Yip, H. T. Huang, L. M. Zhou, K. Y. Xie, Y. Wang, T. H. Feng, J. S. Li and W. Y. Tam, *Adv. Mater.*, 2011, **23**, 5624–5628.
- 27 E. Hendry, T. Carpy, J. Johnston, M. Popland, R. Mikhaylovskiy, A. J. Laphorn, S. M. Kelly, L. D. Barron, N. Gadegaard and M. Kadodwala, *Nat. Nanotechnol.*, 2010, **5**, 783–787.
- 28 K. Yao and Y. M. Liu, *Nanoscale*, 2018, **10**, 8779–8786.
- 29 Y. R. Liu, Z. L. Wu, D. W. Armstrong, H. Wolosker and Y. B. Zheng, *Nat. Rev. Chem.*, 2023, **7**, 355–373.

- 30 H. Lee, S. M. Dellatore, W. M. Miller and P. B. Messersmith, *Science*, 2007, **318**, 426–430.
- 31 J. Sedó, J. Saiz-Poseu, F. Busqué and D. Ruiz-Molina, *Adv. Mater.*, 2013, **25**, 653–701.
- 32 J. H. Zhao, H. Q. Wang, Y. H. Cai, J. J. Zhao, Z. D. Gao and Y. Y. Song, *ACS Sens.*, 2024, **9**, DOI: [10.1021/acssensors.4c00137](https://doi.org/10.1021/acssensors.4c00137).
- 33 S. Cong, Y. Y. Yuan, Z. G. Chen, J. Y. Hou, M. Yang, Y. L. Su, Y. Y. Zhang, L. Li, Q. W. Li, F. X. Geng and Z. G. Zhao, *Nat. Commun.*, 2015, **6**, 7800.
- 34 E. Feng, T. T. Zheng, X. X. He, J. Q. Chen, Q. Y. Gu, X. He, F. H. Hu, J. H. Li and Y. Tian, *Angew. Chem., Int. Ed.*, 2023, **62**, e202309249.